

## BIOCHEMISTRY

# Dimeric structures of quinol-dependent nitric oxide reductases (qNORs) revealed by cryo-electron microscopy

Chai C. Gopalasingam<sup>1</sup>, Rachel M. Johnson<sup>2,3</sup>, George N. Chiduzi<sup>1</sup>, Takehiko Tosha<sup>4</sup>, Masaki Yamamoto<sup>4</sup>, Yoshitsugu Shiro<sup>5</sup>, Svetlana V. Antonyuk<sup>1</sup>, Stephen P. Muench<sup>2,3</sup>, S. Samar Hasnain<sup>1\*</sup>

Copyright © 2019  
The Authors, some  
rights reserved;  
exclusive licensee  
American Association  
for the Advancement  
of Science. No claim to  
original U.S. Government  
Works. Distributed  
under a Creative  
Commons Attribution  
License 4.0 (CC BY).

Quinol-dependent nitric oxide reductases (qNORs) are membrane-integrated, iron-containing enzymes of the denitrification pathway, which catalyze the reduction of nitric oxide (NO) to the major ozone destroying gas nitrous oxide (N<sub>2</sub>O). Cryo-electron microscopy structures of active qNOR from *Alcaligenes xylosoxidans* and an activity-enhancing mutant have been determined to be at local resolutions of 3.7 and 3.2 Å, respectively. They unexpectedly reveal a dimeric conformation (also confirmed for qNOR from *Neisseria meningitidis*) and define the active-site configuration, with a clear water channel from the cytoplasm. Structure-based mutagenesis has identified key residues involved in proton transport and substrate delivery to the active site of qNORs. The proton supply direction differs from cytochrome c-dependent NOR (cNOR), where water molecules from the cytoplasm serve as a proton source similar to those from cytochrome c oxidase.

## INTRODUCTION

Bacterial nitric oxide reductases (NORs) are membrane-integrated, iron-containing enzymes that are involved in microbial denitrification, where soluble nitrogen oxides (e.g., nitrate) are sequentially reduced to liberate nitrogen (N<sub>2</sub>) into the atmosphere (1). NORs catalyze the reduction of two molecules of nitric oxide (NO) to nitrous oxide (N<sub>2</sub>O), using two protons and two electrons to cleave the N—O bond and concurrent N—N bond formation (2, 3):  $2\text{NO} + 2\text{H}^+ + 2\text{e}^- \rightarrow \text{N}_2\text{O} + \text{H}_2\text{O}$ . NORs are part of the heme-copper oxidase superfamily (HCO) (4) and are composed of two subdivisions based on their electron donor: cytochrome c-dependent NOR (cNOR) and quinol-dependent NOR (qNOR). cNORs have been extensively studied and consist of a complex of NorB and NorC, with the latter subunit containing heme c that acts as the electron donor to the binuclear center consisting of a high-spin heme b<sub>3</sub> and a nonheme iron (Fe<sub>B</sub>) in NorB (3, 5). Because oxygen-reducing HCO members (like cytochrome c oxidase) create a proton electrochemical gradient by pumping protons across the membrane (and by taking protons from the negative phase) (6, 7), it was unexpected to find that with cNORs, the protons were taken up from the periplasmic side, indicating a non-electrogenic reaction (8–10).

In contrast, qNORs are single subunit enzymes (NorZ), in which electrons are supplied by menaquinol. qNORs are found not only in denitrifying organisms but also in various pathogenic species (3,11,12), many of which lack the full denitrifying apparatus, bringing to attention the role of qNORs in detoxification. NO has long been

identified as a key signaling molecule, playing an important part in smooth muscle relaxation (13) and blood vessel dilation (14). NO is also produced in macrophages upon response to infectious agents (15), and *Neisseria meningitidis* shows depleted survival in nasopharyngeal tissue when qNOR is knocked out (11). NO is known to inhibit several metalloenzymes within bacteria, such as aconitase (16) and NADH (reduced form of nicotinamide adenine dinucleotide) dehydrogenase (17), and therefore, the presence of qNOR in nondenitrifying organisms seems to be that of defense rather than energy conservation. Thus, substantial efforts have been put toward structural analysis, where the x-ray crystal structure of qNOR from the thermophile *Geobacillus stearothermophilus* (GsqNOR) is determined to a resolution of 2.5 Å, revealing a monomeric structure and indicating the presence of an ordered water channel toward the binuclear center from the cytoplasmic side (18). It has been suggested that the water channel acts in tandem with protonable residues to provide a proton-conducting channel toward the binuclear center, akin to the evolutionarily related K pathway of cytochrome c oxidases (19). However, the incorporation of a non-native zinc at the nonheme catalytic iron site rendered the enzyme inactive. qNOR from *N. meningitidis* (NmqNOR) yielded an active enzyme, but its crystallographic structure showing a monomer could only be determined at a relatively low resolution of ~4.5 Å, where most of the side-chain configurations could not be defined (20).

Despite the fact that the subunit composition of cNOR and qNOR is different, there are conserved structural similarities. The NorB portion of cNOR is homologous to the C terminus of qNOR, and although it lacks heme c in the hydrophilic region, it retains a similar fold to the NorC subunit of cNOR. Both share a low-spin heme b and a high-spin heme b<sub>3</sub>, with a calcium ion bridging the propionates of the respective heme groups, akin to the phylogenetically related cbb<sub>3</sub> oxidase (21). This apparent structural similarity does not extend to either the electron source or the provision of protons required for catalysis. It is hypothesized that qNORs may act in a similar manner to the bd-type quinol oxidase (22), where proton

<sup>1</sup>Molecular Biophysics Group, Institute of Integrative Biology, Faculty of Health and Life Sciences, University of Liverpool, Liverpool L69 7ZB, UK. <sup>2</sup>School of Biomedical Sciences, Faculty of Biological Sciences, University of Leeds, Leeds LS2 9JT, UK. <sup>3</sup>Astbury Centre for Structural and Molecular Biology, University of Leeds, Leeds LS2 9JT, UK. <sup>4</sup>RIKEN SPring-8 Center, 1-1-1 Kouto, Sayo, Hyogo 679-5148, Japan. <sup>5</sup>Graduate School of Life Science, University of Hyogo, 3-2-1 Kouto, Kamigori, Ako, Hyogo 678-1297, Japan.

\*Corresponding author. Email: s.s.hasnain@liv.ac.uk

transfer from the cytoplasmic side is coupled to quinol oxidation (proton release) to the outside of the membrane.

We have purified highly active qNOR from *Alcaligenes xylosoxidans* (AxqNOR), a Gram-negative  $\beta$ -proteobacterium that is equipped with denitrification enzymes, in line with its role as an environmental organism found in well water and moist soil (23). *A. xylosoxidans* is considered an opportunistic pathogen and has been implicated in nosocomial infections (24, 25), is found in patients with cystic fibrosis (26), and is also thought to be a multidrug-resistant organism (26, 27). Here, we have used these preparations to obtain high-resolution structures for the functional wild-type qNOR and its activity-enhanced mutant (Val<sup>495</sup>Ala) by single-particle cryo-electron microscopy (cryo-EM) to local resolutions of 3.7 and 3.2 Å, respectively. Cryo-EM structures unexpectedly revealed AxqNOR to be a dimer. We thus determined a low-resolution (9 Å) cryo-EM structure of active NmQNOR, which is also revealed as a dimer establishing the functional unit of qNORs. A structure-guided mutational study of AxqNOR has allowed us to identify key residues that control and regulate proton and substrate access and thus catalysis.

## RESULTS

### Cryo-EM structural determination of AxqNOR

We explored the structural determination of AxqNOR by single-particle cryo-EM, given the recent achievements in solving sub-100-kDa membrane protein complexes (28, 29). Although AxqNOR preparations had shown a monomer-dimer equilibrium similar to other qNORs, as crystallographic structures of GsqNOR and NmQNOR had revealed them to be monomers [molecular weight (MW), ~85 kDa], it was considered that the AxqNOR monomer on its own would be relatively small for a high-resolution EM structure determination. To facilitate the cryo-EM structural analysis of AxqNOR, we prepared fusion partner constructs to increase the MW of the monomer (96 kDa) to help with the alignment of particles during processing. Guided by information from protein disorder servers, we truncated the C terminus of AxqNOR and fused several different fusion partners for expression trials. AxqNOR fused with apocytochrome b<sub>562</sub> [BRIL (30)], AxqNOR-BRIL, yielded membrane fractions with high NO consumption rates relative to the total protein content and was chosen for structural studies. Purified AxqNOR-BRIL showed a similar NO consumption to wild-type AxqNOR (284 ± 14 versus 291 ± 6 μmol NO min<sup>-1</sup> μmol<sup>-1</sup> qNOR). An exploratory cryo-EM dataset revealed that the particles had a preference toward the carbon edges, with only a low level of clumping present. This likely reflects the “halo” effect that some detergent-solubilized samples exhibit upon freezing, where thinner ice is observed in the center of the hole and becomes thicker toward the edge (31). A small test dataset of ~1200 micrographs produced an initial ~7 Å reconstruction, revealing a previously unseen dimeric form of the protein. Subsequently, a larger dataset (3213 micrographs) was collected thereafter (table S1), of which the particles produced two-dimensional (2D) class averages with visible secondary structure elements, showing a dimeric AxqNOR enveloped by a large micelle. The BRIL portion was less clear, possibly due to its flexibility. Note that no monomeric qNOR classes could be generated from the large particle set, highlighting the fact that the samples are dominated by the dimeric species. Data were processed, with C2 symmetry imposed, providing a structure with a global resolution of 3.9 Å [estimated using the gold standard Fourier shell correlation (FSC) = 0.143 criterion (32)], where local resolution

valued the core of the protein calculated at 3.7 Å. Because the BRIL density was at significantly lower resolution, it was omitted during model building, leaving just the AxqNOR model.

The dimeric AxqNOR is related by a twofold symmetry axis and exhibits a similar overall structure to those of other qNORs, with 14 transmembrane helices (TMHs) and an  $\alpha$ -helical hydrophilic region (Fig. 1A). The heme b<sub>3</sub> and Fe<sub>B</sub> ligating ligands are present on TMHVIII, TMHIX, and TMHXII, where the heme b ligands are present on TMHXII and TMHIV (Fig. 1B). The map showed helix pitches and density for bulky side chains, consistent with the estimated resolution, with several hydrophobic interactions between TMHII of each respective molecule, where Leu<sup>240</sup>, Leu<sup>241</sup>, and Ile<sup>244</sup> act to stabilize the interhelical interaction (Fig. 1C). It is evident that TMHII is a key player in maintaining the AxqNOR dimer, and its importance is discussed in more detail below. In contrast, GsqNOR and NmQNOR were considered to be monomers in the crystal structure. Although inactive monomeric GsqNOR is present in the asymmetric unit, a reexamination of the high-resolution crystallographic structure by PISA (Protein Interfaces, Surfaces and Assemblies) (33) shows that it also probably forms a dimer in the crystal lattice (Fig. 2A), preserving the helical interface. In addition, GsqNOR shows a number of residues on the periplasmic helical region that could also contribute to the dimeric interface (Fig. 2B). The equivalent region in AxqNOR revealed no such favorable interactions (Fig. 2C), despite the fact that the dimer interface area is similar to that in GsqNOR (2278 Å<sup>2</sup> versus 2237 Å<sup>2</sup>, calculated by PISA). However, several charged residues, such as Arg<sup>120</sup> and Glu<sup>121</sup>, may interact at some point, despite the lack of Glu<sup>121</sup> side-chain density (Fig. 2D). The oligomeric status of active NmQNOR was assessed by obtaining a cryo-EM dataset of wild-type NmQNOR. The data produced a 9 Å resolution structure, indicating the enzyme to be a dimer (fig. S1).

### Catalytic site arrangement reveals altered glutamate conformation

The arrangement of the metal centers, namely, the electron-accepting heme b, the propionate bridging Ca<sup>2+</sup>, and the binuclear center of heme b<sub>3</sub> and Fe<sub>B</sub>, is largely similar to those of GsqNOR and NmQNOR, aside from the heme b<sub>3</sub> iron to Fe<sub>B</sub> distance. The densities of heme b<sub>3</sub>, Fe<sub>B</sub>, and their respective ligands (His<sup>486</sup>, His<sup>537</sup>, His<sup>538</sup>, and His<sup>629</sup>) are well defined, where additional conserved residues (Tyr<sup>638</sup> and Gly<sup>603</sup>) provide structural support to Glu<sup>490</sup> and His<sup>629</sup>, respectively (Fig. 3A). Previous structures of active NORs, including cNOR, have shown the heme b<sub>3</sub> Fe to Fe<sub>B</sub> distance to be between 3.2 and 3.9 Å [for NmQNOR (20) and *Pseudomonas aeruginosa* cNOR (PacNOR) (5), respectively], whereas in AxqNOR, the distance is 4.1 Å. In GsqNOR, the distance was 4.8 Å, albeit with zinc instead of iron and with the heme b having been reduced by x-ray exposure (Fig. 3B). An important area of ambiguity in previous structures of qNORs was the side-chain orientation of Glu<sup>490</sup> (Glu<sup>512</sup> in GsqNOR) because zinc was found in the GsqNOR structure (rendering it inactive) and side-chain density could not be resolved with the NmQNOR structure. In PacNOR, the corresponding residue Glu<sup>211</sup> ligates the nonheme iron, while in GsqNOR, it is not a ligand for zinc. The AxqNOR structure contains the correct nonheme metal at the binuclear center (Fe<sub>B</sub>), but the density for the carboxyl group of Glu<sup>490</sup> suggests a different conformation for the side chain compared to GsqNOR and PacNOR, with the carboxyl group approximately 3.5 Å from the His<sup>486</sup> NE2 atom (Fig. 3, C and D). This may reflect a genuine difference in proton delivery pathways between the qNOR (as represented by

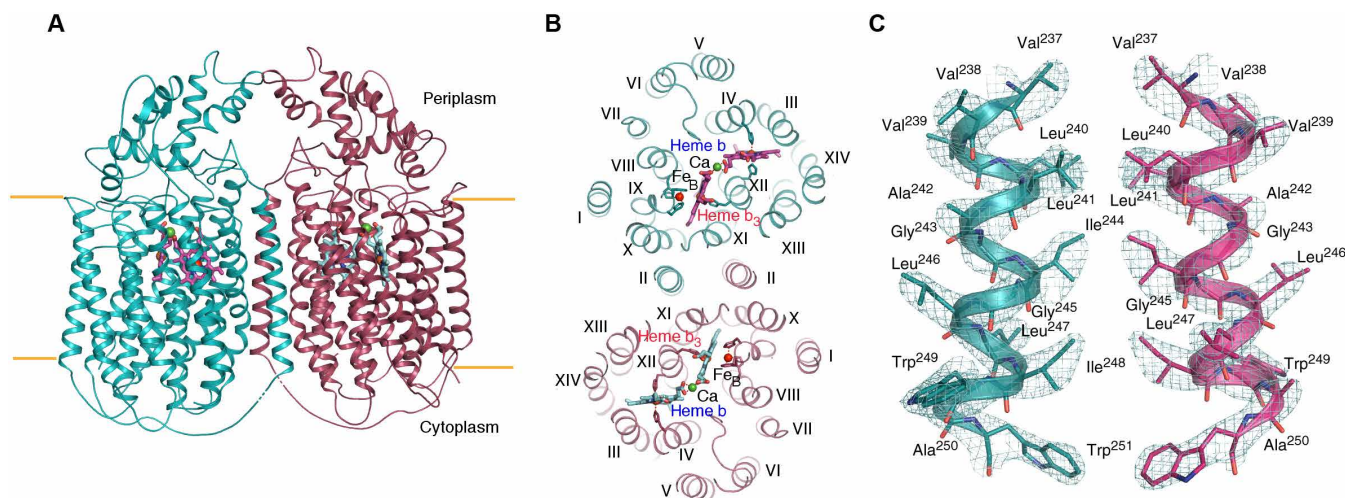


**Fig. 1. Overall structure of AxqNOR and interhelical dimer interactions.** (A) Dimeric AxqNOR in plane of the lipid bilayer (orange lines) colored by chain (A in teal and B in maroon), with heme groups denoted as purple and cyan sticks. (B) AxqNOR viewed from the periplasmic side showing transmembrane helices numbered with roman numerals, with heme and nonheme iron ( $\text{Fe}_b$ ) ligating histidines shown as sticks. Calcium is shown as green spheres, and  $\text{Fe}_b$  is shown as red spheres. (C) Hydrophobic interactions between TMHII of each respective Val<sup>495</sup>Ala molecule with the density map contoured at  $7\sigma$  around the residues, with the wild-type exhibiting a consistent arrangement.

the structure of active AxqNOR) and the cNOR (as represented by the structure of active PacNOR) because the latter receives protons from the periplasm via Glu<sup>280</sup> (Glu<sup>559</sup> in AxqNOR) (5).

### A 3.2 Å structure of an activity-enhanced Val<sup>495</sup>Ala in AxqNOR

An analysis of residues believed to be functionally important in qNORs (vide infra) in the context of the cryo-EM structure of wild-type AxqNOR was done to design and test a number of mutants. One of the mutants, Val<sup>495</sup>Ala, revealed an enhanced activity (by twofold) compared to wild type and was thus chosen for cryo-EM structure determination. A total of 227,000 particles were used in the final refinement (C2 symmetry), with a global resolution of 3.3 Å and a local resolution at 3.2 Å. Upon docking the wild-type EM model into the map, the mutation was clearly visible (Fig. 4A). A notable difference was the poor density of Glu<sup>494</sup> side chain, which, in the wild-type AxqNOR, was resolved to be facing toward Asn<sup>600</sup>, forming a hydrogen bond (Fig. 4A). The Val<sup>495</sup>Ala mutation appears to have increased conformational flexibility of Glu<sup>494</sup>. However, the overall structure of Val<sup>495</sup>Ala-BRIL is largely similar to that of the wild type, with some additional density between the dimer interface assigned as detergent molecules, which were used in solubilization [dodecyl maltoside (DDM)]. The density for the saccharide portion was clear for only half of the molecules and was left for visualization. These molecules are stabilized by Val<sup>230</sup> and His<sup>224</sup> of TMHII (seen in multiple conformations). Val<sup>615</sup> of TMHXI from the opposing molecule also interacts with the acyl tail of the detergent, providing a way to stabilize the dimer interface (Fig. 4B). Density, which appeared to be phospholipid-like, was also seen near the dimer interface, with one phosphatidylethanolamine molecule providing an anchor between TMHII of one molecule and surrounding helices of the other molecule through Phe<sup>598</sup> and Phe<sup>680</sup> (Fig. 4C). In addition, a lipid molecule (truncated to fit the density) was seen closer to the periplasmic surface, where His<sup>692</sup> potentially interacts between the phosphate head group and the acyl tail of the lipid, and also Met<sup>231</sup> of TMHII in proximity to the acyl tail (Fig. 4D).

### Water-mediated proton transfer in AxqNOR

As a result of the improved resolution of the structure of the Val<sup>495</sup>Ala mutant, several new features could be resolved; most notably, a number of water molecules lining the polar channel from the cytoplasmic side to the binuclear site could be seen (Fig. 5A). Several mutants were thus generated on the basis of both sequence conservation (fig. S4) and known structural data, which were then tested for NO reduction under anaerobic conditions. Metal content analysis showed that all mutants had a minimum of 60% of Fe compared to wild type, with optical spectra of most mutants in the Soret region [maximum absorbance at 410 nm ( $A_{410}$ )] in the oxidized state, indicative of a nonperturbed heme environment (fig. S5).  $A_{410}/A_{280}$  ratios of mutants ranged from 0.73 to 0.80 (wild type at 0.70). A closer examination of a residue near the proposed proton entry site (Arg<sup>255</sup>) reveals a water molecule between Glu<sup>572</sup> and Arg<sup>255</sup>, which may act as a proton entry point. Glu<sup>572</sup>Ala had a slightly enhanced activity compared to the wild type, which, considering its proximity to a water molecule and Arg<sup>255</sup>, was unexpected. Both Arg<sup>255</sup> and Glu<sup>572</sup> show relatively weak conservation among qNORs (fig. S6), although a charged residue usually resides in these positions. This may explain why Glu<sup>572</sup>Ala mutants showed little change in NO reduction activity, or it may be that Glu<sup>572</sup> is bypassed during proton transfer. The sequential triple mutant in the aforementioned region (Lys<sup>257</sup>Ala-Glu<sup>258</sup>Ala-Glu<sup>259</sup>Ala) revealed similar consumption rates to the wild-type enzyme, ruling out any significant involvement of these residues in proton entry. Glu<sup>258</sup> and Glu<sup>259</sup> were not observed in the map for wild-type AxqNOR, although the main chain could be resolved in the mutant map. Mutation of the highly conserved Tyr<sup>638</sup> to Phe, which provides structural support to the Glu<sup>490</sup> backbone carbonyl oxygen, did not severely affect the activity. In contrast, mutations of a number of residues located between the middle of the hydrophilic channel and the active site resulted in a substantial loss of activity. Ser<sup>523</sup>, with a conservation of ~30%, showed a ~70% loss of activity (Fig. 5B) upon mutation to alanine, which we suggest arises from the loss of a water molecule that may pass through the flexible Glu<sup>569</sup> (mutants of which we could not express) and Ser<sup>523</sup>. Mutations of



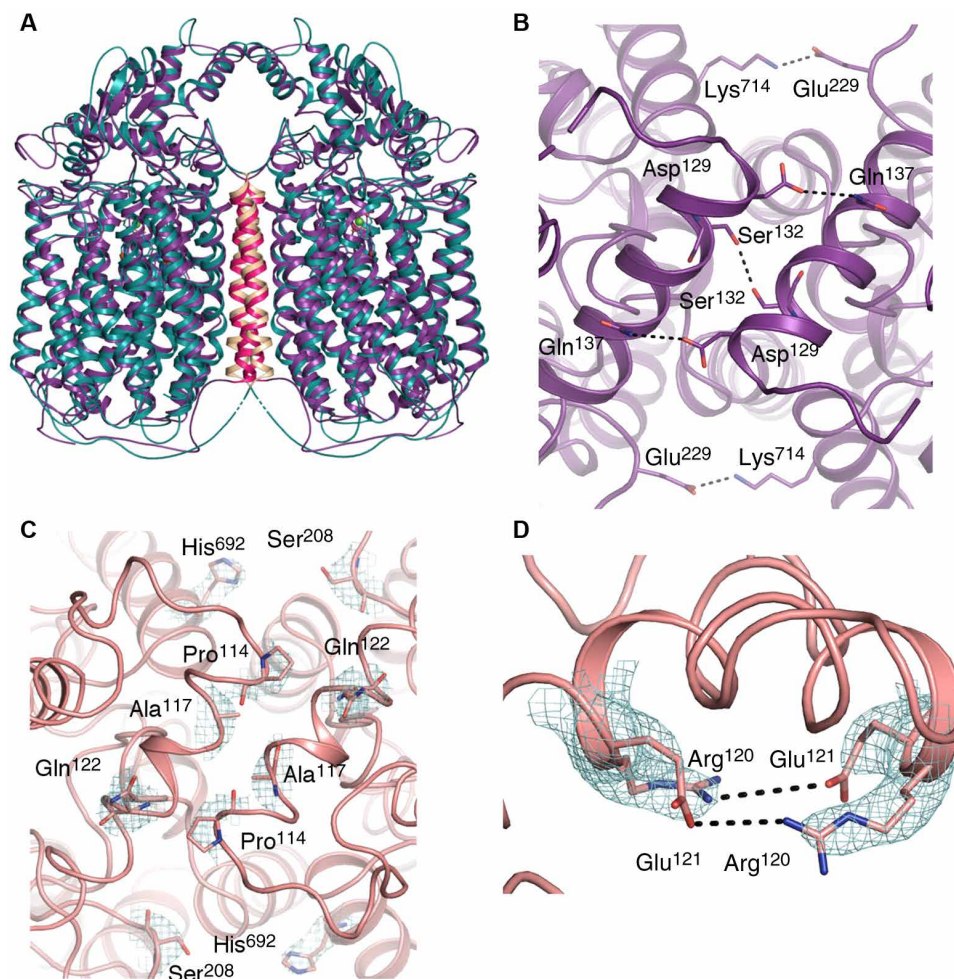


**Fig. 2. Comparison of qNOR dimers and potential soluble interface interactions.** (A) Alignment of AqxNOR (teal) and the dimeric GsqNOR assembly (purple) via PISA. The structures align relatively well despite an overall RMSD of 2.35 Å; dimer mediating TMHII of GsqNOR and AqxNOR are colored in red and gold, respectively. (B) Potential interactions between the GsqNOR monomers in the dimer, as determined by PISA, shown from the periplasmic side, with residues shown as purple sticks. All interactions are  $\leq 4$  Å in bond length. Most of the interactions could occur via a periplasmic helical region, with Glu<sup>229</sup> and Lys<sup>714</sup> located on TMHIX and TMHX of opposing molecules, respectively. (C) Equivalent residues in AqxNOR (mutant structure) contoured with density at 5σ showing no feasible interactions. (D) Potential interactions between Arg<sup>120</sup> and Glu<sup>121</sup> of opposing AqxNOR molecules, where the density was contoured at 4σ for the side chains and the Glu<sup>121</sup> side chain could not be resolved.

Glu<sup>490</sup>, Glu<sup>494</sup>, and Asn<sup>600</sup> (based on sequence alignment of 224 qNOR sequences; the former is fully conserved, while the latter two are 99%, possibly from alignment inaccuracies due to varying gaps) resulted in over 90% loss of activity, providing evidence of their importance in qNOR functionality. The oxidized optical spectra of S523A were slightly perturbed at the Soret region, with absorbance at 411 nm (fig. S5). These are positioned along the proton delivery channel to the active site, where one of the glutamates, Glu<sup>494</sup>, interacts with Asn<sup>600</sup> by a hydrogen bond in the wild-type structure (Fig. 5C). Glu<sup>494</sup> in the 3.3 Å AqxNOR-Val<sup>495</sup>Ala structure exhibits a loss of density, with Asn<sup>600</sup> maintaining its position, yet no water molecules were found in the vicinity. The results of the Glu<sup>494</sup> mutation are consistent with a previous observation that the corresponding residue in NmQNOR was important for proton delivery (20). A water molecule was found ligating the carboxyl group of Glu<sup>490</sup> and Glu<sup>559</sup> (the higher-resolution AqxNOR-Val<sup>495</sup>Ala structure provides clear density of Glu<sup>559</sup>), which is not the case in GsqNOR, as this water does not ligate to the equivalent residues Glu<sup>512</sup> and Glu<sup>581</sup> (Fig. 5D).

The loss of activity for Glu<sup>490</sup>Ala variant in AqxNOR, likely due to the loss of the water molecule and thus the proton source, is consistent with GsqNOR Glu<sup>512</sup>Ala (18), although whether the Glu<sup>512</sup> ligates water in the active state is not known. Overlaying the GsqNOR water channel region with AqxNOR-Val<sup>495</sup>Ala equivalent region shows a more continuous “chain” of waters in the higher-resolution (2.5 Å) GsqNOR structure (Fig. 5E). Several waters are in proximity to those found in GsqNOR, namely, between Glu<sup>572</sup> and Arg<sup>255</sup>, Glu<sup>569</sup> and Thr<sup>498</sup>, and Glu<sup>490</sup> and Glu<sup>559</sup>, providing support to the idea that AqxNOR probably uses protons from the cytoplasmic side for catalytic NO reduction.

### A putative substrate access channel

We conducted a search of potential channels within our AqxNOR structures using CAVER (34) to reveal whether any relevant channels could pertain to substrate entry and delivery to the active site. Starting the search from the active site, three potential candidates were found to be plausible (Fig. 6, A and B), two of which pass by Val<sup>485</sup>

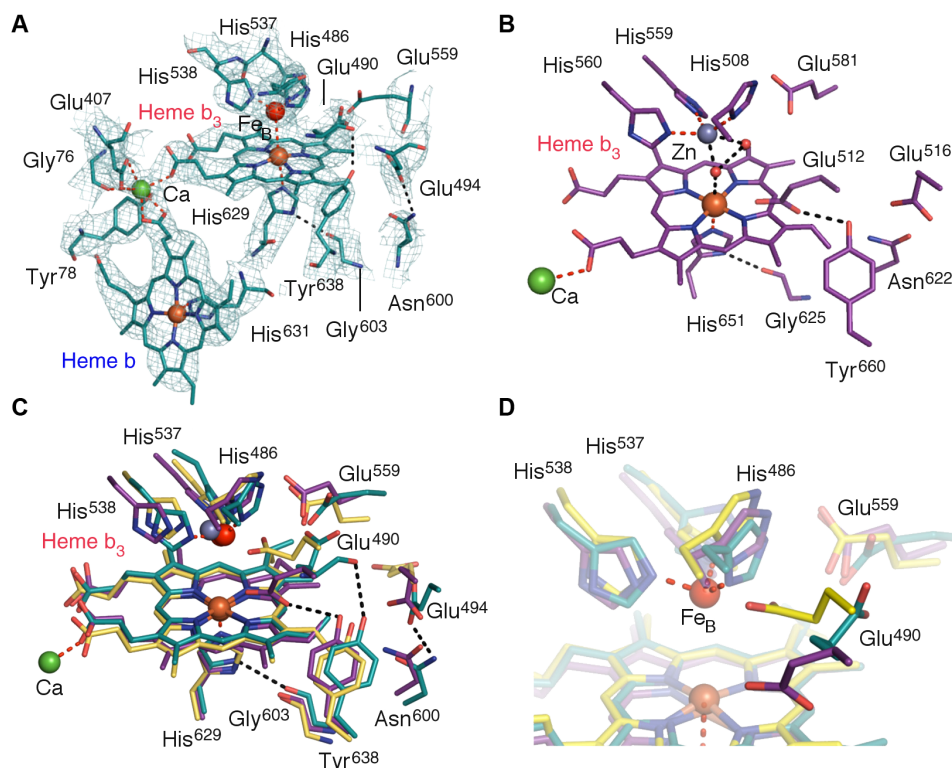


**Fig. 3. Active-site configurations in NORs.** (A) Binuclear center and corresponding density of AqxNOR with  $\text{Fe}_\text{B}$  (red sphere) coordinated by His<sup>486</sup>, His<sup>537</sup>, and His<sup>538</sup>, where Glu<sup>490</sup> facing away from  $\text{Fe}_\text{B}$  with calcium (green sphere) is ligated by heme b and heme  $\text{b}_3$  propionates, Glu<sup>407</sup>, Tyr<sup>78</sup>, and Gly<sup>76</sup> (the latter three residues are highly conserved in qNORs). Tyr<sup>638</sup> and Gly<sup>603</sup> provide additional structural support to the Glu<sup>490</sup> backbone carbonyl oxygen and His<sup>629</sup> ND1 atom, respectively. (B) Binuclear center of GsqNOR with zinc and water molecules shown as gray and red spheres, respectively. (C) Comparison of side-chain conformations (numbered according to AqxNOR) viewed from above the binuclear center in AqxNOR (teal), GsqNOR (purple), and PacNOR (yellow). Zinc is shown as a gray sphere, while  $\text{Fe}_\text{B}$  is colored red. (D) Zoomed-in view of the binuclear center, highlighting the Glu<sup>490</sup> orientation of GsqNOR, AqxNOR, and PacNOR, colored as in (C).

(~7 Å from  $\text{Fe}_\text{B}$ ) en route to the active site from the bilayer. Given the knowledge that Val<sup>206</sup> in PacNOR is implicated in NO transport and is found in the same spatial position as Val<sup>485</sup>, we mutated Val<sup>485</sup> to alanine to ascertain whether it can facilitate NO transport or inhibit it. The Val<sup>485</sup>Ala mutant of AqxNOR exhibited a ~70% loss of activity, signifying its role in NO delivery. The substitution to a smaller side chain may be expected to widen the channel, potentially allowing less constraint for NO to access the catalytic site. Yet, the Val<sup>206</sup>Trp mutant of PacNOR caused loss of NO consumption in vitro, which is suggested to be due to the increase in bulk, creating a barrier near the active site (35). Having a residue of sufficient hydrophobicity and appropriate size is a key component in determining NO access to the active site. Closer inspection of the structure showed that the highly conserved Val<sup>489</sup> (fig. S4) lies beneath Val<sup>485</sup>, which may act in tandem with Val<sup>485</sup> to funnel NO toward the active site. GsqNOR channel analysis revealed two channels that overlap a similar spatial location in AqxNOR, which may indicate a conserved role of these hydrophobic tunnels in substrate transfer (Fig. 6C). Comparison with structures of PacNOR [and its complex with  $\text{cd}_1\text{NiR}$  (35)] and *Thermus thermophilus* cytochrome  $\text{ba}_3$  (36) suggest that similar hydrophobic channels exist for gas diffusion from outside the membrane to the active site.

## DISCUSSION

Highly active preparations of AqxNOR were obtained but did not yield well-diffracting crystals <7 Å, despite substantial efforts. Given

a relatively small MW of the monomer (~85 kDa) for cryo-EM experiments, it was fused with apocytochrome  $\text{b}_{562}$  [BRIL(30)], raising the MW of the monomer to ~96 kDa. This facilitated structural determination by cryo-EM, unexpectedly revealing a dimeric AqxNOR (predicted MW with BRIL, ~190 kDa). The high quality of the structures suggests that BRIL may have also stabilized AqxNOR, something often seen in the crystallographic structure determination of G protein (heterotrimeric guanine nucleotide-binding protein)-coupled receptors (37). Attachment of BRIL at the C terminus of AqxNOR (TMHXIV) did not alter the enzymatic activity. Despite the high quality of maps, BRIL could not be resolved to high resolution, although it is clear from both the 2D classes and 3D reconstruction that its spatial location is well away from the dimer interface and it displays a large degree of flexibility (fig. S2). The resolution obtained here compares favorably against complexes of larger sizes, using a similar number of particles in the final refinement (52,000 to 57,000), e.g., cytochrome  $\text{bc}_1$  (~500 kDa, 4.4 Å) (38) and alternative complex III (~316 kDa, 3.9 Å) (39). The Val<sup>495</sup>Ala-BRIL mutant provided a structure at a higher resolution of 3.3 Å using 227,000 particles, with local resolution estimates from ResMap (40) ranging to as high as 2.5 Å (fig. S3).

The dimeric structure of a qNOR observed here raised an important question regarding the oligomeric status of the functionally important form of the previously crystallographically studied qNORs. A cryo-EM data collection of wild-type *NmqNOR* provided a 9 Å structure demonstrating it to be dimer, suggesting that crystallization

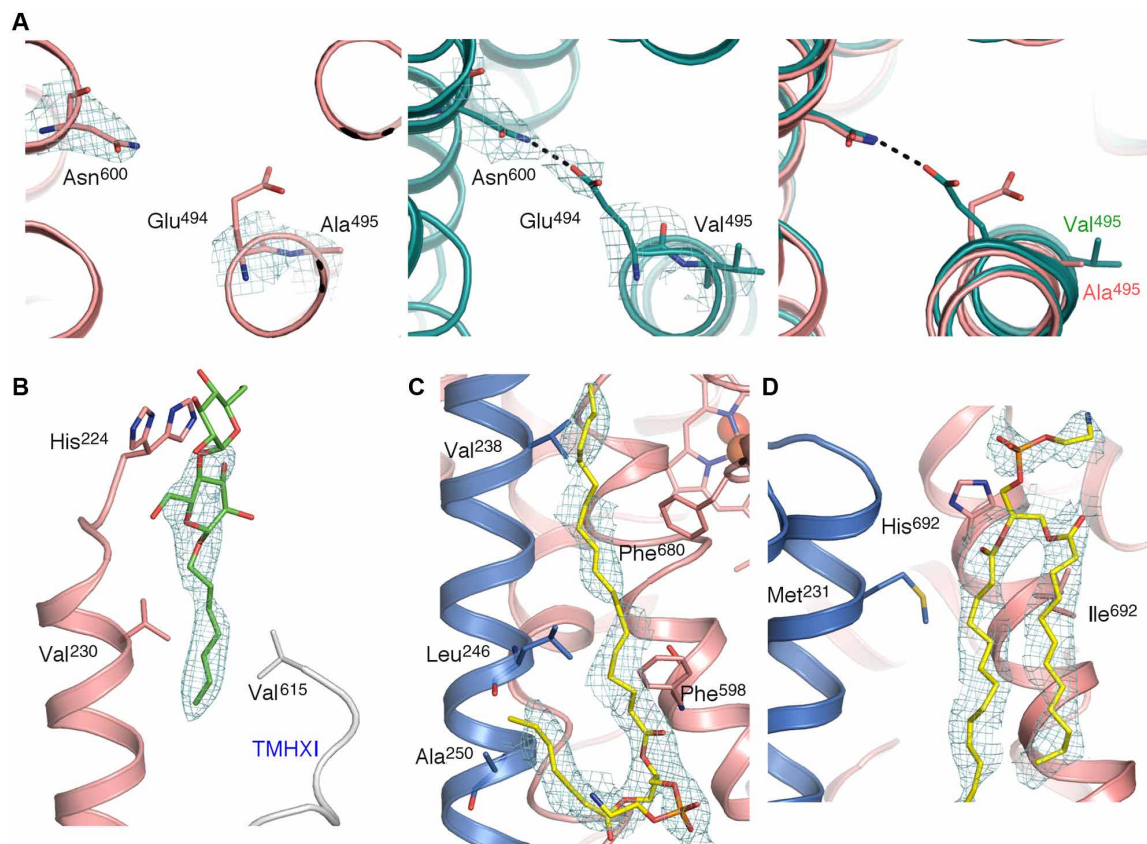


**Fig. 4. Val<sup>495</sup>Ala-BRIL structural features and lipid-protein interactions.** (A) Insight into the structural impact of the Val<sup>495</sup>Ala mutation on the orientation of Glu<sup>494</sup>: left, density for Val<sup>495</sup>Ala contoured at 4 $\sigma$  with Glu<sup>494</sup> side chain not visible in the density map; middle, wild-type structure density contoured at 4 $\sigma$  (Glu<sup>494</sup>-Asn<sup>600</sup> salt bridge shown in black); right, aligned structures highlighting the differences between side-chain orientations (wild type in teal and Val<sup>495</sup>Ala in pink). (B) The possible truncated DDM molecule (depicted as green stick) at the dimer interface, mediated by His<sup>224</sup>, is shown in two conformations near the detergent head group, while highly conserved valine residues on TMHII (Val<sup>230</sup> and Val<sup>237</sup>) and Pro<sup>613</sup> from the opposing molecule (TMHII) may stabilize the acyl chain. Symmetry-related DDM is not shown for clarity. (C) Phosphatidylethanolamine (PE) molecule, shown as a yellow stick, found toward the cytoplasmic end of the protein, with the acyl tail running close to TMHII residues (Val<sup>238</sup>, Leu<sup>246</sup>, and Ala<sup>250</sup>) of one qNOR chain (in blue) and Phe<sup>598</sup> and Phe<sup>680</sup> of another chain (in pink). (D) PE molecule (yellow stick) found on the periplasmic side of the dimer interface, stabilized by Met<sup>231</sup> of TMHII, with His<sup>692</sup> interacting electrostatically with the propionate group.

may have preferentially selected the monomeric species. Both AxqNOR cryo-EM structures show that TMHII, which is absent in cNORs, maintains the dimeric form of AxqNOR with several hydrophobic interactions between TMHII of each respective molecule, acting to stabilize the interhelical interaction. Lipids are known to facilitate and be indispensable for oligomerization and functioning of several membrane protein complexes [e.g., leucine transporter (41), cytochrome c oxidase (42), and cytochrome bc<sub>1</sub> (43)]. The presence of lipids around the dimer interface may be a key physiological feature in qNORs, and the presence of detergent at the dimer boundary might be a surrogate for host lipids, because the hydrophobic residues on TMHII and Val<sup>615</sup> from the opposing molecule interacted with the acyl tail and could conceivably do so with lipids. Because monomeric qNOR is also isolated during purification, the addition of detergent may replace some weakly bound lipids, which may alter the dimer affinity, causing a greater propensity of monomers or preferential selection during crystallization conditions. The absence of monomers in the cryo-EM data suggests that dominant species of active AxqNOR and NmQNOR, from which EM grids were made, is dimeric.

Although the replacement of nonheme Fe<sub>B</sub> with zinc in GsqNOR hampered the elucidation of a structure-function relationship in

qNOR, comparing the structure of inactive GsqNOR with that of active AxqNOR provides valuable information in reaching the structure-property relationship that is generic for qNORs. A proton entry site for qNORs has been proposed to be on a cytoplasmic loop, composed of several charged residues. Our triple mutant (Lys<sup>257</sup>-Glu<sup>258</sup>A-Glu<sup>259</sup>A) had a similar activity to the wild type, which was similar in the case of NmQNOR with the Glu<sup>259</sup> point mutations. The enhanced resolution for AxqNOR from the structure of the Val<sup>495</sup>Ala-BRIL mutant has allowed us to map out a number of water molecules, with Arg<sup>255</sup> potentially acting as a starting point for proton transfer from the cytoplasmic solvent toward the binuclear site. The significantly enhanced activity of Val<sup>495</sup>Ala is likely to arise from alleviating proton transfer as the rate-limiting step. This most likely results from increased conformational dynamics of Glu<sup>494</sup>, which shuttles the proton toward the catalytic pocket. The importance of several residues located between the binuclear center and the cytoplasmic surface is indicated in this study, namely, Ser<sup>523</sup> and Asn<sup>600</sup>, in maintaining a putative proton transfer channel with possible partners Glu<sup>569</sup> and Glu<sup>494</sup>, respectively. Ser<sup>523</sup>, despite its relatively low conservation (30% among 224 sequences), exhibits a significant loss of activity upon mutation. The conformer of Glu<sup>569</sup> is facing



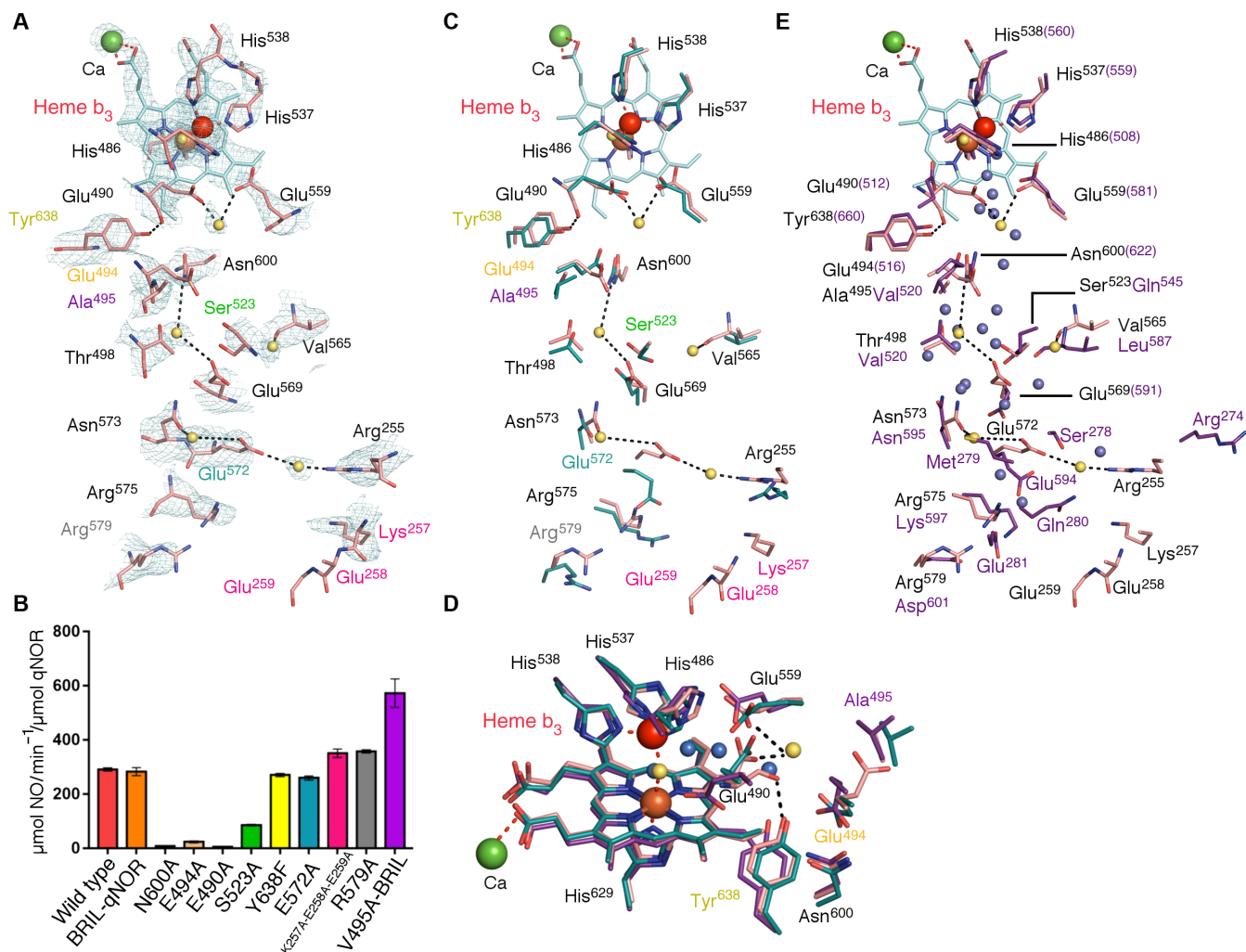


**Fig. 5. Putative water channel in AqxNOR and effects of mutagenesis on NO reductase activity.** (A) Residues [colored labels according to bar graph in (B), with the exception of Asn<sup>600</sup> and Glu<sup>490</sup>] and accompanying densities lining the proposed proton transfer in Val<sup>495</sup>Ala AqxNOR (pink sticks) from the cytoplasmic side to the binuclear center (calcium and Fe<sub>B</sub> are shown as green and red spheres, respectively). Water molecules are shown as yellow spheres and traverse from Arg<sup>255</sup> toward Glu<sup>490</sup>. (B) Bar graph detailing the effect of structure-guided mutagenesis on NO reduction rates, performed in anaerobic conditions for each variant. Colored bars indicate the mean consumption rate ( $n = 3$ ), with SEM bars shown for each variant as black lines. (C) Alignment of the wild-type AqxNOR (teal sticks) and Val<sup>495</sup>Ala proton transfer pathway indicating the variation in some side-chain conformations, notably with Glu<sup>572</sup> and Glu<sup>494</sup>. (D) Comparison of the binuclear site among wild-type AqxNOR (teal), Val<sup>495</sup>Ala AqxNOR (pink), and GsqNOR (purple), with residue numbers from AqxNOR. Calcium is shown as a green sphere, Fe<sub>B</sub> in wild-type AqxNOR is shown as an orange sphere, and Fe<sub>B</sub> in Val<sup>495</sup>Ala AqxNOR Fe<sub>B</sub> is shown as a red sphere. Water molecules from Val<sup>495</sup>Ala are depicted as yellow spheres, while those from GsqNOR are shown in blue. Waters bridging the nonheme metal to the heme b<sub>3</sub> (oxo ligand) and in between Glu<sup>490</sup> and Glu<sup>559</sup> show similar locations in both GsqNOR and Val<sup>495</sup>Ala AqxNOR structures. (E) GsqNOR water channel (residues in purple sticks, water shown by gray spheres) aligned against Val<sup>495</sup>Ala AqxNOR equivalent region (residues in pink, water shown as yellow spheres). Residues show higher conservation further up the channel, with GsqNOR having a continuous chain of water molecules toward the binuclear site.

toward Ser<sup>523</sup> in our structures, which may indicate a functional role of Glu<sup>569</sup>-Ser<sup>523</sup> in proton transport. The drastic effect on activity due to the mutation of Glu<sup>494</sup> in both AqxNOR and NmQNOR (Glu<sup>498</sup>) suggests its critical functional role in qNOR. However, the equivalent mutant in *Paracoccus denitrificans* cNOR (Glu<sup>202</sup>) shows only ~60% loss of activity when heterologously expressed in *Escherichia coli* JM109 cells (44, 45), consistent with its potential role in providing a sufficient electronegative environment to lower the redox potential of the heme b<sub>3</sub> iron compared to the other heme groups (46). It should be noted that Glu<sup>490</sup> and Glu<sup>494</sup> variants in AqxNOR exhibited ~70% of Fe compared to wild type. This may contribute to a lower activity, but the oxidized and reduced optical spectra of all

variants were identical to those of wild type (fig. S5), suggesting that iron is not depleted from the Fe<sub>B</sub> site preferentially. Contrary to cNOR, proton transfer pathway in qNORs likely originates from the cytoplasmic side, with Glu<sup>494</sup> playing an important part in proton transport.

The mechanism of NO reduction in membrane-integrated NORs has been the subject of intense investigation, and the structural determination of PacNOR was a significant step. A key element was the proposed flexibility of Glu<sup>211</sup> (coordinating Fe<sub>B</sub>) to accommodate two NO molecules in the active site. Glu<sup>211</sup> (Glu<sup>490</sup> in AqxNOR) is proposed to accept protons from Glu<sup>280</sup> (Glu<sup>559</sup> in AqxNOR), causing protonation and possible dissociation from Fe<sub>B</sub>, allowing NO binding

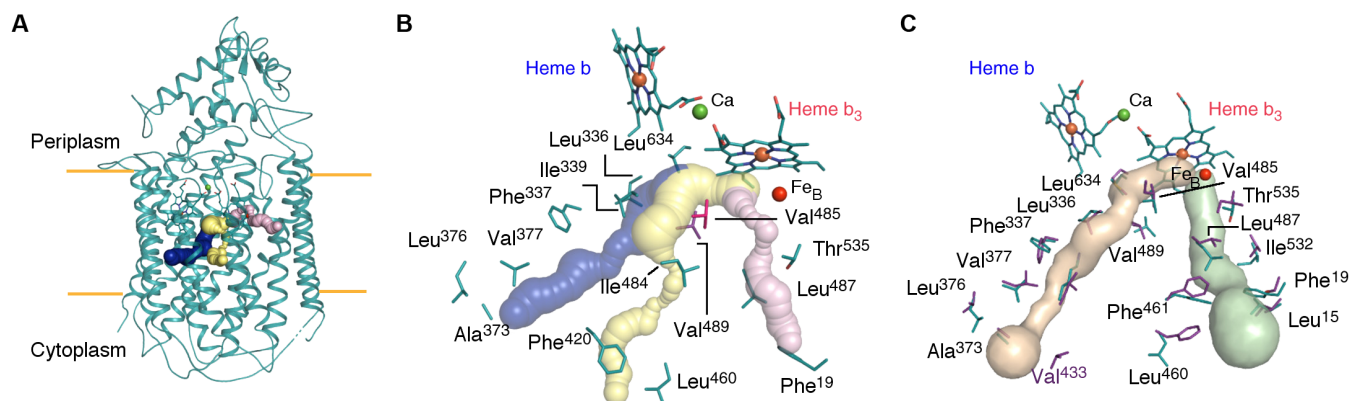


**Fig. 6. Putative NO diffusion pathways in wild-type AxqNOR.** (A) Location of proposed hydrophobic channels in wild-type AxqNOR protruding from the bilayer to the binuclear site, based on CAVER analysis, shown as blue, yellow, and pink tunnels. (B) Location of hydrophobic channels viewed from the periplasmic side lined with residues situated along the tunnels (heme groups are shown as teal sticks, with calcium and Fe<sub>B</sub> shown as green and red spheres, respectively). Val<sup>485</sup> and Val<sup>489</sup> are colored in pink and purple sticks. (C) GsqNOR hydrophobic tunnels [from Matsumoto *et al.* (18)] with residue numbers from AxqNOR (teal) and GsqNOR (purple) aligned, showing similar spatial location and residue type, with Val<sup>485</sup> being replaced with Ile<sup>507</sup> in GsqNOR.

[assuming that an increase in the Fe-Fe distance to at least 4.4 Å occurs, as suggested by Richardson and colleagues (2)], while structures of the ligand analog-bound forms of PacNOR showed that Glu<sup>211</sup> coordinated to Fe<sub>B</sub> even in the presence of the ligand. Glu<sup>490</sup> in AxqNOR unequivocally faces away from Fe<sub>B</sub>, suggesting that Glu<sup>490</sup> and its equivalents in (active) qNORs do not act as an Fe<sub>B</sub> ligand and instead ligate a water molecule along with Glu<sup>559</sup>. The directionality of proton transfer to the terminal glutamates in qNOR differs from cNOR, as Glu<sup>494</sup> in AxqNOR is crucial to activity but the equivalent glutamate in cNOR only loses half its activity when mutated (44), possibly down to periplasmic supplied protons flowing through Glu<sup>280</sup> toward Glu<sup>211</sup>. The precise role of this residue in cNOR is still unclear. It has been suggested that it may be a remnant in the evolutionary pathway in acquiring protons from the cytoplasmic end in cytochrome oxidases because it is (roughly) positioned at the end of the K pathway (47).

Molecular dynamic simulations of the crystal structure of PacNOR-cd<sub>1</sub> NiR complex suggested that NO transfer may occur primarily via the lipid bilayer and not via the active sites of each enzyme (35). Given the lipophilicity of NO, the migration of NO toward and into the lipid bilayer is feasible. Depending on where AxNiR may interact (with either AxqNOR, the lipid bilayer, or both), the use of either channel seems plausible for providing access to NO released from AxNiR. We identified Val<sup>485</sup> to be an important residue in guiding NO to the active site of AxqNOR, but as the Val<sup>485</sup>Ala mutant exhibited a loss of 70% activity, additional inputs may be present. In view of the need to detoxify NO rapidly, having multiple entry points may be an advantage. The passage of NO and its binding to qNOR may also need to be barrier-less, consistent with a fast rate constant as established in cNOR (48). The tunnel analysis suggests that Leu<sup>376</sup> and Phe<sup>420</sup> may act as input points, yet the intersections of the tunnels before the active site consist of Val<sup>485</sup> and Val<sup>489</sup>. Because Val<sup>489</sup> is strongly conserved (fig. S6), it may compensate for the loss of Val<sup>485</sup> to continue shuttling NO. A computation study on PacNOR investigated NO diffusion and found that several migration pathways exist (termed dominant and alternate), where migration of NO is ~10-fold lower using the alternate route than using the dominant pathway (49). Several of the routes include conserved residues found in our tunnel analysis (Val<sup>285</sup>, Ile<sup>484</sup>, Leu<sup>336</sup>, and Leu<sup>487</sup>), which may suggest a generic role in NO transport across NORs. A similar

study on cytochrome ba<sub>3</sub> found hydrophobic tunnels that are located within the bilayer and provide O<sub>2</sub> an area to partition from the aqueous phase, with no significant energetic barriers for O<sub>2</sub> transport (50).

In summary, we solved the structure of wild-type and mutant AxqNOR at local resolutions of 3.7 and 3.2 Å, respectively, by cryo-EM. These structures are the first example that documents dimeric structures of qNORs, providing details on the structural architecture. The active site and putative proton transfer pathway arrangements are revealed at a high enough resolution of an active qNOR. The current structure and mutational results, together with the previous data, suggest that qNORs take up protons from cytoplasmic side, with several water molecules facilitating this to occur. This is in contrast to cNORs, which receive protons from the periplasmic side (5). This redefines the role of qNOR as a respiratory enzyme, and its evolutionary relationship to cytochrome c oxidase, setting qNORs apart from both cNOR and the denitrification enzymes NiR and nitrous oxide reductase, which are not considered to be directly involved in energy conservation.

## MATERIALS AND METHODS

### Construction of AxqNOR-BRIL expression plasmid and site-directed mutants

The AxqNOR-BRIL and Val<sup>495</sup>Ala-BRIL expression plasmid was made by GenScript (Hong Kong), with the AxqNOR gene (NorZ) truncated (Δ747 to Δ763) to accommodate the apocytochrome b<sub>562</sub> [BRIL<sub>562</sub>, Protein Data Bank (PDB) accession code: 1M6T] fusion partner at the C terminus of AxqNOR. The chimeric gene (qNOR-BRIL) was then ligated between the Nde I and Xho I sites of a pET-26b (+) plasmid, allowing a hexa-histidine tag to be attached at the C terminus of BRIL<sub>562</sub>. Site-directed mutants of qNOR were generated using the QuikChange II Kit (Agilent) using the wild-type AxqNOR plasmid as a template vector. Mutations were confirmed by DNA sequencing before use.

### Purification of AxqNOR-BRIL, Val<sup>495</sup>Ala-BRIL, and site-directed mutants

C41 (DE3) *E. coli* cells (Lucigen) were transformed with the expression plasmid and grown in 2xYT media. Upon reaching an A<sub>600</sub> of



~2,  $\delta$ -aminolevulinic acid (Sigma-Aldrich) and  $\text{FeCl}_3$  were added at final concentrations of 200  $\mu\text{M}$ , as well as IPTG (isopropyl- $\beta$ -D-thiogalactopyranoside) was added at a final concentration of 500  $\mu\text{M}$ , to induce overexpression of qNOR-BRIL. Harvested cells were washed in 50 mM tris (pH 7.0) and 150 mM NaCl and then lysed by sonication, before collecting membrane fractions by ultracentrifugation. Membranes (final concentration of 7 mg/ml) were solubilized in 50 mM tris (pH 7.0), 150 mM NaCl, and 1% (v/v)  $\beta$ -DDM (Anatrace) for 2 hours at 4°C. The solubilized material was separated by centrifugation at 40,000 rpm and loaded onto a pre-equilibrated 5-ml HisTrap column (GE Healthcare). The column was subjected to three column volumes worth of washing in 50 mM tris (pH 7.0), 150 mM NaCl, 20 mM imidazole, 0.05% DDM, and then two-column volumes in the same buffer, yet with 35 mM imidazole. The protein was eluted in the same buffer, using 150 mM imidazole instead. Fractions were assessed for purity by SDS-polyacrylamide gel electrophoresis and ultraviolet (UV)-visible spectroscopy (U-3300, Hitachi), with elutions having an  $A_{410}/A_{280}$  ratio of >0.6 being carried forward. After concentration in Amicon Ultra 100K concentrators, qNOR-BRIL was loaded onto a Superdex 200 10/300 Increase (GE Healthcare) column equilibrated in 50 mM tris (pH 7.0), 150 mM NaCl, and 0.05% (v/v) decyl-thio-maltoside (DTM) (Anatrace). Fractions with  $A_{410}/A_{280} > 0.7$  were concentrated to 20 mg/ml and flash-frozen in liquid nitrogen, before storage at -80°C. Val<sup>495</sup>Ala-BRIL was purified in the same manner, except that buffers were at pH 7.5. Site-directed mutants were purified in a similar manner to AxqNOR-BRIL, except that, at gel filtration, 0.05% DDM was used instead of DTM.

### UV-visible absorption spectroscopy

Absorption spectra were recorded on U-3300 spectrophotometer (Hitachi). AxqNOR samples were diluted in gel filtration buffer and subjected to measurements for the oxidized state. An excess of sodium dithionite was added to the oxidized samples (final concentration, ~1 mM) and remeasured to obtain fully reduced spectra.

### Enzymatic activity measurements

Before enzyme activity measurements, samples were subjected to inductively coupled plasma optical emission spectrometry (ICP-OES) analysis with an ICP-OES 5110 instrument (Agilent) to ascertain metal content. qNOR activity was measured using a Clark-type electrode fitted with an ISO-NO Mark II system (WPI). All reaction components (aside from glucose oxidase and catalase) were made anaerobic by replacing the atmosphere of the vials with  $\text{N}_2$ . The assay buffer contained 50 mM Na-citrate (pH 6.0), 0.05% DDM or DTM, 100 mM D-glucose, 10  $\mu\text{g ml}^{-1}$  glucose oxidase, and 10  $\mu\text{g ml}^{-1}$  catalase. Glucose, glucose oxidase, and catalase were added to scavenge any oxygen left in the reaction vessel. Sodium ascorbate (1 mM) and phenazine methosulfate (10  $\mu\text{M}$ ) acted as an electron donation system. A 2 mM NO saturated solution [50 mM Na-citrate (pH 6.0)] was made and added at a final concentration of 20  $\mu\text{M}$ . NO consumption was started by addition of the protein at a final concentration of 0.2  $\mu\text{M}$ .

### Cryo-EM sample preparation and data collection

qNOR-BRIL was diluted to 3 mg/ml, and 3  $\mu\text{l}$  of aliquots was applied on glow-discharged Quantifoil Au R1.2/1.3 holey carbon grids. Grids were plunge-frozen in liquid ethane using Vitrobot Mark IV (FEI), with grids blotted for 6 s, and a blot force of 6, maintained at 100%

humidity and 4°C. Grids were then loaded into an FEI Titan Krios TEM (Astbury Biostructure Laboratory, University of Leeds), operating at 300 kV, equipped with a K2 Summit detector (Gatan). Automated data collection was performed with EPU software at a magnification of  $\times 75,000$ , using a defocus range of -1.5 to -3.5  $\mu\text{m}$ . A total of 3213 micrographs were collected with a pixel size of 1.07 Å. A total dose of 65  $\text{e}^-/\text{Å}^2$  was acquired by using a dose rate of 6.21  $\text{e}^- \text{pixel}^{-1} \text{s}^{-1}$  across 40 frames for 12 s of total exposure time. AxqNOR Val<sup>495</sup>Ala-BRIL was prepared in the same way as the wild type, except that the sample (5 mg/ml) was used with Quantifoil Cu R1.2/1.3 holey carbon grids. Val<sup>495</sup>Ala-BRIL grids were loaded into an FEI Titan Krios at Electron Bio-Imaging Centre (eBIC) (Diamond Light Source) operating at 300 kV, equipped with a K2 Summit detector (Gatan). Automated data collection was performed with EPU software at a magnification of  $\times 47,710$ , using a defocus range of -1 to -3  $\mu\text{m}$ . A total of 1803 micrographs were collected with a pixel size of 1.05 Å. A total dose of 49  $\text{e}^-/\text{Å}^2$  was acquired by using a dose rate of 4.16  $\text{e}^- \text{pixel}^{-1} \text{s}^{-1}$  across 40 frames for 10 s of total exposure time.

### Image processing

All image processing was performed in RELION 3.0(51). Beam-induced motion and drift correction were performed using RELION 3.0 own implementation. Contrast Transfer Function (CTF) estimation was carried out using CTFFIND-4.1 (52), with CTF correction carried out on non-dose-weighted micrographs, with further data processing done on dose-weighted micrographs. Around 2000 particles were manually picked and extracted to generate initial 2D classes that were used as templates for automatic particle picking. Approximately 700,000 particles were picked and sorted before 2D classification on ~540,000 particles was carried out. The best 2D classes were chosen to make an initial model, which was then low pass-filtered to 60 Å and used for 3D classification. Several rounds of 3D classification were performed, with the best class out of three being taken forward for the next round of classification. A total of 56,134 particles yielded a refined map at a global resolution of 4.1 Å with C2 symmetry, using a soft mask encompassing the protein and detergent micelle. CTF refinement and Bayesian particle polishing improved the resolution to 3.9 Å, where local resolutions suggest that the core of the protein is 3.7 Å. Tighter masks failed to increase the resolution of the final map. Resolutions were estimated by the gold standard FSC = 0.143 criterion, while local resolutions were valued using RELION. Val<sup>495</sup>Ala was processed in a similar fashion to the wild type, albeit with motion correction carried out using RELION 3.0 implementation. From ~600,000 auto-picked particles, multiple rounds of 2D and 3D classification led to 227,000 particles being used in the final reconstruction to attain a resolution of 3.7 Å, with C2 symmetry. After CTF refinement and Bayesian particle polishing, the resolution improved to 3.5 Å. A tight mask excluding the micelle was used in postprocessing to improve the resolution further to 3.3 Å, with a local resolution at 3.2 Å. Resolutions were estimated by the gold standard FSC = 0.143 criterion, while local resolutions were valued using RELION. ResMap (40) was used to assess slice through volume local resolution estimates.

### Model building, refinement, and validation

The high-resolution GsqNOR (PDB accession code: 3AYF) structure (33% sequence identity) was fitted into the locally filtered map using the Chimera's "Fit in Map" function (53), which then served as a template to manually build the AxqNOR structure in Coot. The

Arp/Warp web server (<https://arpwarp.embl-hamburg.de/>) was used as an additional aid in manual model building in difficult regions (solvent-exposed loops and periplasmic helical region). As the density of the BRIL was far less detailed than that of the qNOR molecules, only qNOR was built into the maps. The resulting structure was then refined with secondary structure and custom geometry restraints around the metal centers (heme b,  $\text{Ca}^{2+}$ , heme b<sub>3</sub>, and Fe<sub>B</sub>) and their respective ligands, using the phenix.real\_space\_refine program in the Phenix suite (54). Models were checked in Coot to identify any regions that needed correcting, based on both Coot and MolProbity validation statistics. For Val<sup>495</sup>Ala, B-factor sharpening was performed on the local resolution filtered map, using a value of  $-147 \text{ \AA}^2$ , determined from running the bfactor\_plot.py script in RELION 3.0. The structure of Val<sup>495</sup>Ala was solved by fitting the wild-type AqxNOR model into the map and adjusting/refining the model as described before. Figures were made using Chimera and PyMOL.

## SUPPLEMENTARY MATERIALS

Supplementary material for this article is available at <http://advances.sciencemag.org/cgi/content/full/5/8/eaax1803/DC1>

Fig. S1. 3D cryo-EM reconstruction of wild-type NmqNOR.

Fig. S2. Summary of cryo-EM data collection for wild-type and Val<sup>495</sup>Ala AqxNOR.

Fig. S3. Henderson-Rosenthal plots of qNOR datasets and local resolution slice through plots.

Fig. S4. Multiple sequence alignment of selected qNORs.

Fig. S5. Oxidized and dithionite reduced spectra of selected AqxNOR variants.

Fig. S6. Residue probability chart of qNORs.

Table S1. Cryo-EM data collection parameters and refinement statistics.

Table S2. AqxNOR putative proton transfer channel site-directed mutants' conservation and relative activities.

## REFERENCES AND NOTES

- W. G. Zumft, Cell biology and molecular basis of denitrification. *Microbiol. Mol. Biol. Rev.* **61**, 533–616 (1997).
- N. J. Watmough, S. J. Field, R. J. L. Hughes, D. J. Richardson, The bacterial respiratory nitric oxide reductase. *Biochem. Soc. Trans.* **37**, 392–399 (2009).
- J. Hendriks, A. Oubrie, J. Castresana, A. Urbani, S. Gemeinhardt, M. Saraste, Nitric oxide reductases in bacteria. *Biochim. Biophys. Acta Bioenerg.* **1459**, 266–273 (2000).
- F. L. Sousa, R. J. Alves, M. A. Ribeiro, J. B. Pereira-Leal, M. Teixeira, M. M. Pereira, The superfamily of heme-copper oxygen reductases: Types and evolutionary considerations. *Biochim. Biophys. Acta Bioenerg.* **1817**, 629–637 (2012).
- T. Hino, Y. Matsumoto, S. Nagano, H. Sugimoto, Y. Fukumori, T. Murata, S. Iwata, Y. Shiro, Structural basis of biological  $\text{N}_2\text{O}$  generation by bacterial nitric oxide reductase. *Science* **330**, 1666–1670 (2010).
- S. Yoshikawa, K. Muramoto, K. Shinzawa-Itoh, Proton-pumping mechanism of cytochrome C oxidase. *Annu. Rev. Biophys.* **40**, 205–223 (2011).
- S. Iwata, C. Ostermeier, B. Ludwig, H. Michel, Structure at 2.8 Å resolution of cytochrome c oxidase from *Paracoccus denitrificans*. *Nature* **376**, 660–669 (1995).
- J. H. M. Hendriks, A. Jasaitis, M. Saraste, M. I. Verkhovskiy, Proton and electron pathways in the bacterial nitric oxide reductase. *Biochemistry* **41**, 2331–2340 (2002).
- J. Reimann, U. Flock, H. Lepp, A. Honigsmann, P. Adelroth, A pathway for protons in nitric oxide reductase from *Paracoccus denitrificans*. *Biochim. Biophys. Acta* **1767**, 362–373 (2007).
- U. Flock, F. H. Thorndyck, A. D. Matorin, D. J. Richardson, N. J. Watmough, P. Adelroth, Defining the proton entry point in the bacterial respiratory nitric-oxide reductase. *J. Biol. Chem.* **283**, 3839–3845 (2008).
- T. M. Stevanin, J. W. B. Moir, R. C. Read, Nitric oxide detoxification systems enhance survival of *Neisseria meningitidis* in human macrophages and in nasopharyngeal mucosa. *Infect. Immun.* **73**, 3322–3329 (2005).
- A. M. Lewis, S. S. Matzdorf, J. L. Endres, I. H. Windham, K. W. Bayles, K. C. Rice, Examination of the *Staphylococcus aureus* nitric oxide reductase (saNOR) reveals its contribution to modulating intracellular NO levels and cellular respiration. *Mol. Microbiol.* **96**, 651–669 (2015).
- L. A. Blatter, W. G. Wier, Nitric oxide decreases  $[\text{Ca}^{2+}]_i$  in vascular smooth muscle by inhibition of the calcium current. *Cell Calcium* **15**, 122–131 (1994).
- C. Farah, L. Y. M. Michel, J.-L. Balligand, Nitric oxide signalling in cardiovascular health and disease. *Nat. Rev. Cardiol.* **15**, 292–316 (2018).
- J. MacMicking, Q. W. Xie, C. Nathan, Nitric oxide and macrophage function. *Annu. Rev. Immunol.* **15**, 323–350 (1997).
- M. C. Kennedy, W. E. Antholine, H. Beinert, An EPR investigation of the products of the reaction of cytosolic and mitochondrial aconitases with nitric oxide. *J. Biol. Chem.* **272**, 20340–20347 (1997).
- E. Clementi, G. C. Brown, M. Feelisch, S. Moncada, Persistent inhibition of cell respiration by nitric oxide: Crucial role of S-nitrosylation of mitochondrial complex I and protective action of glutathione. *Proc. Natl. Acad. Sci. U.S.A.* **95**, 7631–7636 (1998).
- Y. Matsumoto, T. Tosha, A. V. Pislakov, T. Hino, H. Sugimoto, S. Nagano, Y. Sugita, Y. Shiro, Crystal structure of quinol-dependent nitric oxide reductase from *Geobacillus stearothermophilus*. *Nat. Struct. Mol. Biol.* **19**, 238–245 (2012).
- J. Koepke, E. Olkhova, H. Angerer, H. Müller, G. Peng, H. Michel, High resolution crystal structure of *Paracoccus denitrificans* cytochrome c oxidase: New insights into the active site and the proton transfer pathways. *Biochim. Biophys. Acta Bioenerg.* **1787**, 635–645 (2009).
- N. Gonska, D. Young, R. Yuki, T. Okamoto, T. Hisano, S. Antonyuk, S. S. Hasnain, K. Muramoto, Y. Shiro, T. Tosha, P. Adelroth, Characterization of the quinol-dependent nitric oxide reductase from the pathogen *Neisseria meningitidis*, an electrogenic enzyme. *Sci. Rep.* **8**, 3637 (2018).
- S. Buschmann, E. Warkentin, H. Xie, J. D. Langer, U. Ermler, H. Michel, The structure of *cbb3* cytochrome oxidase provides insights into proton pumping. *Science* **329**, 327–330 (2010).
- V. B. Borisov, R. B. Gennis, J. Hemp, M. I. Verkhovskiy, The cytochrome bd respiratory oxygen reductases. *Biochim. Biophys. Acta Bioenerg.* **1807**, 1398–1413 (2011).
- J. B. Spear, J. Fuhrer, B. D. Kirby, *Achromobacter xylosoxidans* (*Alcaligenes xylosoxidans* subsp. *xylosoxidans*) bacteremia associated with a well-water source: Case report and review of the literature. *J. Clin. Microbiol.* **26**, 598–599 (1988).
- C. E. Swenson, R. T. Sadikot, *Achromobacter* respiratory infections. *Ann. Am. Thorac. Soc.* **12**, 252–258 (2015).
- H. Awadh, M. Mansour, O. Aqtash, Y. Shweihat, Pneumonia due to a rare pathogen: *Achromobacter xylosoxidans*, subspecies *denitrificans*. *Case Rep Infect Dis.* **2017** (2017).
- A. Lambiase, M. R. Catania, M. Del Pezzo, F. Rossano, V. Terlizzi, A. Sepe, V. Raia, *Achromobacter xylosoxidans* respiratory tract infection in cystic fibrosis patients. *Eur. J. Clin. Microbiol. Infect. Dis.* **30**, 973–980 (2011).
- M. Yamamoto, M. Nagao, G. Hotta, Y. Matsumura, A. Matsushima, Y. Ito, S. Takakura, S. Ichijima, Molecular characterization of IMP-type metallo-β-lactamases among multidrug-resistant *Achromobacter xylosoxidans*. *J. Antimicrob. Chemother.* **67**, 2110–2113 (2012).
- W. Wang, R. MacKinnon, Cryo-EM structure of the open human *Ether-à-go-go*-related K<sup>+</sup> channel hERG. *Cell* **169**, 422–430.e10 (2017).
- J. Sun, R. MacKinnon, Cryo-EM structure of a KCNQ1/CaM complex reveals insights into congenital long QT syndrome. *Cell* **169**, 1042–1050.e9 (2017).
- R. Chu, J. Takei, J. R. Knowlton, M. Andrykovitch, W. Pei, A. V. Kajara, P. J. Steinbach, X. Ji, Y. Bai, Redesign of a four-helix bundle protein by phage display coupled with proteolysis and structural characterization by NMR and X-ray crystallography. *J. Mol. Biol.* **323**, 253–262 (2002).
- I. Drulyte, R. M. Johnson, E. L. Hesketh, D. L. Hurdiss, C. A. Scarff, S. A. Porav, N. A. Ranson, S. P. Muench, R. F. Thompson, Approaches to altering particle distributions in cryo-electron microscopy sample preparation. *Acta Crystallogr. Sect. D Struct. Biol.* **74**, 560–571 (2018).
- S. H. W. Scheres, S. Chen, Prevention of overfitting in cryo-EM structure determination. *Nat. Methods* **9**, 853–854 (2012).
- E. Krissinel, K. Henrick, Inference of macromolecular assemblies from crystalline state. *J. Mol. Biol.* **372**, 774–797 (2007).
- M. Petřek, M. Otyepka, P. Banáš, P. Košínová, J. Koča, J. Damborský, CAVER: A new tool to explore routes from protein clefts, pockets and cavities. *BMC Bioinformatics* **7**, 316 (2006).
- E. Terasaka, K. Yamada, P.-H. Wang, K. Hosokawa, R. Yamagiwa, K. Matsumoto, S. Ishii, T. Mori, K. Yagi, H. Sawai, H. Arai, H. Sugimoto, Y. Sugita, Y. Shiro, T. Tosha, Dynamics of nitric oxide controlled by protein complex in bacterial system. *Proc. Natl. Acad. Sci. U.S.A.*, 9888–9893 (2017).
- V. M. Luna, Y. Chen, J. A. Fee, C. D. Stout, Crystallographic studies of Xe and Kr binding within the large internal cavity of cytochrome ba 3 from *thermus thermophilus*: Structural analysis and role of oxygen transport channels in the heme–Cu oxidases. *Biochemistry* **47**, 4657–4665 (2008).
- E. Chun, A. A. Thompson, W. Liu, C. B. Roth, M. T. Griffith, V. Katritch, J. Kunken, F. Xu, V. Cherezov, M. A. Hanson, R. C. Stevens, Fusion partner toolchest for the stabilization and crystallization of G protein-coupled receptors. *Structure* **20**, 967–976 (2012).
- K. Ampornpanai, R. M. Johnson, P. M. O'Neill, C. W. G. Fishwick, A. H. Jamson, S. Rawson, S. P. Muench, S. S. Hasnain, S. V. Antonyuk, X-ray and cryo-EM structures of inhibitor-bound cytochrome bc 1 complexes for structure-based drug discovery. *IUCr J* **5**, 200–210 (2018).

39. J. S. Sousa, F. Calisto, J. D. Langer, D. J. Mills, P. N. Refojo, M. Teixeira, W. Kühlbrandt, J. Vonck, M. M. Pereira, Structural basis for energy transduction by respiratory alternative complex III. *Nat. Commun.* **9**, 1728 (2018).
40. A. Kucukelbir, F. J. Sigworth, H. D. Tagare, Quantifying the local resolution of cryo-EM density maps. *Nat. Methods* **11**, 63–65 (2014).
41. K. Gupta, J. A. C. Donlan, J. T. S. Hopper, P. Uzdavinyis, M. Landreh, W. B. Struwe, D. Drew, A. J. Baldwin, P. J. Stansfeld, C. V. Robinson, The role of interfacial lipids in stabilizing membrane protein oligomers. *Nature* **541**, 421–424 (2017).
42. I. Liko, M. T. Degiacomi, S. Mohammed, S. Yoshikawa, C. Schmidt, C. V. Robinson, Dimer interface of bovine cytochrome c oxidase is influenced by local posttranslational modifications and lipid binding. *Proc. Natl. Acad. Sci. U.S.A.* **113**, 8230–8235 (2016).
43. C. Lange, J. H. Nett, B. L. Trumpower, C. Hunte, Specific roles of protein-phospholipid interactions in the yeast cytochrome *bc*<sub>1</sub> complex structure. *EMBO J.* **20**, 6591–6600 (2001).
44. F. H. Thorndyrcroft, G. Butland, D. J. Richardson, N. J. Watmough, A new assay for nitric oxide reductase reveals two conserved glutamate residues form the entrance to a proton-conducting channel in the bacterial enzyme. *Biochem. J.* **401**, 111–119 (2007).
45. G. Butland, S. Spiro, N. J. Watmough, D. J. Richardson, Two conserved glutamates in the bacterial nitric oxide reductase are essential for activity but not assembly of the enzyme. *J. Bacteriol.* **183**, 189–199 (2001).
46. K. L. C. Grönberg, M. D. Roldán, L. Prior, G. Butland, M. R. Cheesman, D. J. Richardson, S. Spiro, A. J. Thomson, N. J. Watmough, A low-redox potential heme in the dinuclear center of bacterial nitric oxide reductase: Implications for the evolution of energy-conserving heme-copper oxidases. *Biochemistry* **38**, 13780–13786 (1999).
47. T. Hino, S. Nagano, H. Sugimoto, T. Tosha, Y. Shiro, Molecular structure and function of bacterial nitric oxide reductase. *Biochim. Biophys. Acta Bioenerg.* **1817**, 680–687 (2012).
48. S. M. Kapetanaki, S. J. Field, R. J. L. Hughes, N. J. Watmough, U. Liebl, M. H. Vos, Ultrafast ligand binding dynamics in the active site of native bacterial nitric oxide reductase. *Biochim. Biophys. Acta* **1777**, 919–924 (2008).
49. P. Mahinthichaichan, R. B. Gennis, E. Tajkhorshid, Bacterial denitrifying nitric oxide reductases and aerobic respiratory terminal oxidases use similar delivery pathways for their molecular substrates. *Biochim. Biophys. Acta* **1859**, 712–724 (2018).
50. P. Mahinthichaichan, R. B. Gennis, E. Tajkhorshid, All the O<sub>2</sub> consumed by *Thermus thermophilus* cytochrome *ba*<sub>3</sub> is delivered to the active site through a long, open hydrophobic tunnel with entrances within the lipid bilayer. *Biochemistry* **55**, 1265–1278 (2016).
51. J. Zivanov, T. Nakane, B. O. Forsberg, D. Kimanius, W. J. H. Hagen, E. Lindahl, S. H. W. Scheres, New tools for automated high-resolution cryo-EM structure determination in RELION-3. *eLife* **7**, e42166 (2018).
52. A. Rohou, N. Grigorieff, CTFIND4: Fast and accurate defocus estimation from electron micrographs. *J. Struct. Biol.* **192**, 216–221 (2015).
53. E. F. Pettersen, T. D. Goddard, C. C. Huang, G. S. Couch, D. M. Greenblatt, E. C. Meng, T. E. Ferrin, UCSF Chimera—a visualization system for exploratory research and analysis. *J. Comput. Chem.* **25**, 1605–1612 (2004).
54. P. V. Afonine, B. K. Poon, R. J. Read, O. V. Sobolev, T. C. Terwilliger, A. Urzhumtsev, P. D. Adams, Real-space refinement in PHENIX for cryo-EM and crystallography. *Acta Crystallogr. Sect. D Struct. Biol.* **74**, 531–544 (2018).

**Acknowledgments:** We would like to acknowledge discussions with R. Eady and K. Muramoto. Wild-type AxqNOR and NmQNOR EM data were collected at the Astbury Biostructure Laboratory with the assistance of R. Thompson (Leeds). We thank Diamond for access and support of the cryo-EM facilities at the UK National eBIC, proposal number EM19832-3, funded by the Wellcome Trust, MRC, and BBSRC. We also thank Y. Chaban (eBIC) for help with data collection for Val<sup>495</sup>Ala AxqNOR. **Funding:** The work on denitrifying enzymes in Liverpool is supported by BBSRC (BB/L006960/1 and BB/N013972/1). C.C.G. is supported by a RIKEN-Liverpool International Programme Associate studentship (awarded to M.Y., S.V.A., and S.S.H.). S.V.A. also thanks SFTC's ASTEC department for financial support to the project. R.M.J. thanks the Wellcome Trust for PhD studentship support (109158/B/15/Z), and the Astbury Biostructure Laboratory is supported through the Wellcome Trust (108466/Z/15/Z). **Author contributions:** C.C.G. expressed, purified, and performed enzymatic assays with the protein samples. R.M.J. and S.P.M. made cryo-EM sample grids and helped set up the data collection for the wild-type structure. C.C.G., R.M.J., and G.N.C. processed the cryo-EM images. C.C.G. and S.V.A. built and refined the models. S.P.M., T.T., M.Y., Y.S., S.V.A., and S.S.H. conceived the study. C.C.G., S.P.M., T.T., Y.S., S.V.A., and S.S.H. prepared the manuscript. All authors read and discussed the results. **Competing interests:** The authors declare that they have no competing interests. **Data and materials availability:** All data needed to evaluate the conclusions in the paper are present in the paper and/or the Supplementary Materials. Wild-type AxqNOR-BRIL cryo-EM map has been deposited in the Electron Microscopy Data Bank under the accession code EMD-4618, with Val<sup>495</sup>Ala-BRIL cryo-EM map deposited under the accession code EMD-4619. Atomic coordinates of the wild-type AxqNOR and Val<sup>495</sup>Ala AxqNOR structures have been deposited to the PDB under accession codes 6QQ5 and 6QQ6, respectively. Additional data related to this paper may be requested from the authors.

Submitted 28 February 2019

Accepted 24 July 2019

Published 28 August 2019

10.1126/sciadv.aax1803

**Citation:** C. C. Gopalasingam, R. M. Johnson, G. N. Chiduzu, T. Tosha, M. Yamamoto, Y. Shiro, S. V. Antonyuk, S. P. Muench, S. S. Hasnain, Dimeric structures of quinol-dependent nitric oxide reductases (qNORs) revealed by cryo-electron microscopy. *Sci. Adv.* **5**, eaax1803 (2019).



## Dimeric structures of quinol-dependent nitric oxide reductases (qNORs) revealed by cryo-electron microscopy

Chai C. Gopalasingam, Rachel M. Johnson, George N. Chiduzza, Takehiko Tosha, Masaki Yamamoto, Yoshitsugu Shiro, Svetlana V. Antonyuk, Stephen P. Muench and S. Samar Hasnain

*Sci Adv* 5 (8), eaax1803.  
DOI: 10.1126/sciadv.aax1803

### ARTICLE TOOLS

<http://advances.sciencemag.org/content/5/8/eaax1803>

### SUPPLEMENTARY MATERIALS

<http://advances.sciencemag.org/content/suppl/2019/08/26/5.8.eaax1803.DC1>

### REFERENCES

This article cites 52 articles, 13 of which you can access for free  
<http://advances.sciencemag.org/content/5/8/eaax1803#BIBL>

### PERMISSIONS

<http://www.sciencemag.org/help/reprints-and-permissions>

Use of this article is subject to the [Terms of Service](#)

---

*Science Advances* (ISSN 2375-2548) is published by the American Association for the Advancement of Science, 1200 New York Avenue NW, Washington, DC 20005. 2017 © The Authors, some rights reserved; exclusive licensee American Association for the Advancement of Science. No claim to original U.S. Government Works. The title *Science Advances* is a registered trademark of AAAS.